Journal of Applied Polymer Science

WILEY

Applied Polymer SCIENCE

RESEARCH ARTICLE OPEN ACCESS

Microstructure Tuning and Performance Enhancement of Polystyrene Foams via Ball-Milled Biochar–Induced Nucleation in Supercritical CO_2-Assisted Extrusion

Apurv Gaidhani | Stephan Edwards | William Z. Xu | Lauren Tribe | Paul Charpentier

Department of Chemical and Biochemical Engineering, University of Western Ontario, London, Ontario, Canada

Correspondence: Paul Charpentier (pcharpen@uwo.ca; pcharpentier@eng.uwo.ca)

Received: 5 November 2025 | **Revised:** 9 January 2026 | **Accepted:** 15 January 2026

Keywords: extrusion | polystyrene | structure–property relationships | synthesis and processing techniques

ABSTRACT

Developing sustainable thermal insulation materials is critical to reducing building energy consumption and greenhouse gas emissions. This study developed lightweight, high-performance polystyrene (PS) composite foams reinforced with wood-derived biochar using a continuous supercritical CO_2 (sc-CO_2) extrusion process. Ball-milled biochar (MBC) with a high surface area and porosity acted as an efficient heterogeneous nucleating agent, resulting in a 40% increase in cell density (4×10^8 cells cm^{-3}) and a narrower cell size distribution (average cell size 75 μm) as compared to pristine PS foams. These refined microstructures reduced thermal conductivity by up to 4% (32 mW/m K) and enhanced specific compressive strength by 75%, reaching 3.8 MPa g cm^{-3}, suitable for load-bearing insulation applications. Transmission electron microscopy (TEM) and micro-computed tomography (CT) confirmed uniform biochar dispersion and preferential localization along cell walls, validating its role in nucleation and reinforcement. The PS-MBC composite foam processed at 20.6 MPa exhibited superior mechanical and thermal performance compared with conventional foams. Overall, this scalable and solvent-free sc-CO_2 foaming approach provides a sustainable pathway to upcycle renewable wood residues into high-performance polymer insulation materials, with improved mechanical reliability, thermal efficiency, and environmental responsibility.

1 | Introduction

Polystyrene (PS) foams are widely used as thermal insulation materials [1] across diverse sectors such as construction [2] and packaging [3] due to their lightweight nature [4, 5], low thermal conductivity [6], and cost-effectiveness [7]. In building applications, extruded polystyrene (XPS) foams help to reduce energy consumption by minimizing heat transfer through walls, roofs, and floors [8]. In cold-climate regions, where heating demands are high, insulation plays a crucial role in lowering energy usage and associated greenhouse gas (GHG) emissions [9–11]. According to a study by Zhao et al. [12], buildings account for nearly 35% of global terminal energy consumption and 38% of energy-related greenhouse gases (GHG) emissions in the world, much of which is linked to space heating in temperate and cold zones [13]. Improving thermal insulation is thus essential for meeting energy efficiency goals and enhancing indoor comfort. Studies have shown that advanced insulation systems can reduce building energy demands by 30%–50%, especially in cold-climate countries such as Canada, Finland, and Norway [14, 15]. These benefits underscore the importance of developing sustainable, high-performance composite insulation materials that combine thermal performance with environmental responsibility to reduce GHG emissions of buildings.

Biochar is a lightweight, carbon-rich residue produced via pyrolysis of biomass and it possesses key physical characteristics that make it a promising nucleating agent and reinforcing filler in polymer foams. Biochar is an attractive filler for building materials due to its naturally low thermal conductivity, porous

structure, sustainability, and cost-effectiveness [16–18]. Its porous framework, combined with low heat transfer characteristics, enhances insulation performance by interrupting pathways for thermal bridging [19] In Canada, vast quantities of lignocellulosic residues from forestry and wood industries present both a waste management and environmental challenge [20, 21]; valorizing these residues into biochar for polymer composite foams provides a sustainable solution [22]. The role of biochar as a nucleating agent, as well as its contributions to thermal and sound insulation in polymer foams, was reviewed in detail in our previous study [23]. Adeniyi et al. [24] reported that PS–biochar composites had reduced thermal conductivity up to 30 wt% loading due to biochar's low conductivity, but higher loadings increased the thermal conductivity via pore-induced thermal bridging when heat capacity rose with biochar content. Similarly, Jian et al. [25] achieved a 13% thermal conductivity reduction in PS foams with up to 1.5 wt% coconut-shell biochar, with little change in specific thermal conductivity. Another study by Adeniyi et al. [26] reported that incorporating 30 wt% biochar improved the hardness of PS biochar composites by 43% as compared to pure PS. Ball milling of biochar significantly increases its specific surface area and improves its compatibility with the polymer matrix [27]. Ogunsona et al. reported that a finely milled biochar led to improved interfacial adhesion and composite performance in terms of tensile strength and heat distortion temperature [28, 29]. Likewise, composites of polyamide 6 reinforced with finely milled biochar showed increased tensile modulus and heat deflection temperature due to improved adhesion and dispersion [30].

Recent studies by Adeniyi et al. [26, 31] have explored the use of biochar as a filler in polystyrene composites to enhance mechanical and thermal characteristics; however, such studies remain limited, and the integration of biochar into polystyrene foams, particularly using pilot-scale, continuous supercritical CO_2 (sc-CO_2) foaming processes to improve thermal insulation performance, has not yet been reported. Most other studies have examined polyurethane or biodegradable polylactic acid (PLA) systems, typically using batch foaming setups that are less representative of continuous large-scale manufacturing conditions [32]. These limitations present an opportunity to investigate biochar's dual functionality as a low-cost, sustainable filler and as a nucleating agent in scalable PS foam systems [33, 34]. Prior studies have demonstrated the use of conventional carbon-based fillers such as graphene nanoplatelets (GNP), flake graphite (FG), and carbon nanotubes (CNTs) to reduce the thermal conductivity of PS foams. Jian et al. [25] reported that incorporating graphene and CNTs at a loading of 1 wt% during PS foam extrusion resulted in a ~20% reduction in thermal conductivity compared to pristine PS foam, achieving values as low as 32 mW/m K. Similarly, Almeida et al. [35] incorporated FG into PS foams at a higher loading of up to 15 wt%, reducing the thermal conductivity from 44 mW/m K to approximately 33 mW/m K. However, unlike conventional carbon fillers such as GNP, FG, and CNTs, biochar can be derived from abundant forestry residues and waste biomass, offering additional environmental benefits including low cost, renewability, and long-term carbon sequestration alongside potential thermal-insulation performance gains. Furthermore, pilot scale continuous sc-CO_2 foaming mimics real-world production, facilitating scalability, cost-effective optimization, and risk reduction for industrial-scale manufacturing [36].

This study aims to develop lightweight, mechanically robust, and thermally efficient biochar PS composite foams using sc-CO_2 extrusion foaming, aligning with sustainability and circular economy goals. Wood-derived biochar, produced from renewable lignocellulosic residues such as oak and maple sawdust, was incorporated at 2.5 wt% loading, with particle size tailored via ball milling to enhance specific surface area and nucleation efficiency. The effects of the particle size of biochar and sc-CO_2 pressure (17.3 and 20.6 MPa) were systematically evaluated to understand their influence on cell morphology, thermal conductivity, and compressive strength. Advanced imaging techniques, including TEM and micro-CT, were employed to study biochar dispersion and its preferential localization within the foam structure. Particular emphasis was placed on correlating microstructural parameters such as cell size, cell density, and uniformity with macroscopic thermal and mechanical performance. The findings offer valuable insights for the design and production of eco-efficient composite insulation foams suitable for energy-efficient building applications.

2 | Experimentation

2.1 | Materials

Biochar (BC), produced via pyrolysis of maple and oak sawdust, was kindly provided by Airex Energy (Quebec, Canada). Polystyrene (PS 595 T) with a melt flow index (MFI) of 1.6 g/10 min (200°C, 5 kg) and a density of 1.04 g/cm^3 was purchased from TotalEnergies Petrochemicals & Refining (USA). The blowing agent, carbon dioxide (CO_2, 99.9% purity), was supplied by Linde Canada. Talc powder (JetWhite 1HC, 98% purity, median particle size 1.1 μm) was kindly donated by Magris Talc (USA).

2.2 | Extrusion Foaming of PS and PS–Biochar Composites

Extrusion foaming of pristine PS and PS–biochar composites was carried out on a pilot-scale twin-screw extruder (Feininger SHJ-Z36×25, $D = 36$ mm, $L/D = 25$, throughput = 3 kg/h) using sc-CO_2 as the physical blowing agent, injected at two pressures (17.3 and 20.6 MPa). All formulations contained 1 wt% talc as a nucleating agent. The processing procedure, described in detail in our previous work [37] involved a primary compounding stage followed by a secondary foaming stage under reduced temperatures. The detailed temperature profiles and processing parameters are summarized in Table 1.

Virgin PS foamed under these conditions served as the pristine reference sample (designated as PS-0 control). After several extrusion runs with unmilled biochar (BC) loadings ranging from 0 to 7.5 wt% as described in our previous study [38], 2.5 wt% BC foam was selected for the particle size study, as it provided the lowest thermal conductivity while avoiding the severe surface and internal defects observed at higher loadings (see Figure S1). To evaluate the influence of biochar particle size on foam nucleation, milling of BC was carried out before extrusion. Approximately 15 g of BC was introduced into a 125 mL stainless steel milling vessel and subjected to

TABLE 1 | Temperature and processing parameters for PS-biochar foam extrusion.

Feed zone (°C)	Compression zone (°C)	Metering zone (°C)	Die zone (°C)	Screw speed (RPM)	Cooling
190/130	195/195	190/165	140	50	Ambient

Note: Values before and after "/" refer to primary and secondary extrusion stages, respectively.

TABLE 2 | Sample nomenclature for pristine and biochar-reinforced PS foams.

Sample	Biochar type	wt%	Label
Pristine PS	—	0	PS-0 control
Biochar	BC	2.5	BC foam
Ball-milled biochar	MBC	2.5	MBC foam

ball milling for 10 min at 600 rpm. The procedure was performed in two stages, consisting of 5 min of clockwise rotation and 4 min of counterclockwise rotation, with a 60 s rest period between cycles, using a planetary ball mill (Retsch PM200, Germany). Milling was conducted with 30 stainless steel balls (10 mm diameter, 3.87 g each), yielding a total media mass of 615 g and a ball-to-biochar mass ratio of 41:1.

The ball-milled biochar (MBC) was then added in 2.5 wt% to PS, and foaming was conducted using the same extrusion procedure. The sample designations used for pristine and biochar-reinforced PS foams are summarized in Table 2. A schematic overview of the extrusion foaming process is presented in Figure 1.

2.3 | Characterization

2.3.1 | Density and Morphological Analysis

Foam density was calculated using ASTM D1622. Three specimens were tested for each composite foam sample and the average value is reported. The test specimens were rectangular in shape (23 × 8 × 7 mm). The foam skin was carefully removed using a sharp razor blade prior to the measurements and an average of three readings was taken for the final reported value. Expansion ratio of foam (ϕ) was calculated as

$$\phi = \frac{\rho_{\text{unfoamed}}}{\rho_{\text{foamed}}} \tag{1}$$

where ρ_{unfoamed} is the bulk density of the solid polymer composite and ρ_{foamed} is the density of the foam.

Morphological analysis of the PS-biochar composite foams was performed using a scanning electron microscope (SEM, Hitachi Flex SEM 1000 II) operating at a voltage of 5 kV to examine the foam morphologies. The foam samples were freeze-fractured in liquid nitrogen, and observations were carried out along the direction perpendicular to the extrusion at the center of the foam width after removal of the skin. Fiji (ImageJ) software was used for cell size and particle size analysis, utilizing SEM pictures with a magnification ratio of 50. Cell size was calculated as the average diameter of all cells in a SEM picture. Subsequently, the cell density (N_0) was calculated:

$$N_0 = \left(\frac{n}{A}\right)^{\frac{3}{2}} \phi \tag{2}$$

where n is the number of cells in a SEM picture, A is the area of the SEM picture, and N_0 is the number of cells per unit volume. Cell and particle size distribution were plotted using histograms and Gaussian fitting.

2.3.2 | Thermal and Mechanical Properties

Thermal conductivity was measured under steady state conditions using a Heat Flow Meter (HFM) Fox 200 setup plate instrument supplied by TA Instruments and manufactured by LaserComp. Figure S2 depicts a setup of HFM. Thermogravimetric analysis (TGA) was conducted using a Q600 thermogravimetric analyzer (TA Instruments, USA) to evaluate the thermal stability and decomposition behavior of the foams. Measurements were performed from room temperature to 900°C at a constant heating rate of 10°C min^{-1} under both nitrogen and air atmospheres, each supplied at a flow rate of 100 mL min^{-1}. TG curves were obtained to quantify the mass retained as a function of temperature, while derivative thermogravimetric (DTG) curves, computed as the first derivative of the TG curves, were used to determine the mass-loss rates and identify characteristic decomposition stages. Strain-controlled compressive strength tests of the foams were studied using a vertical compression setup, consisting of a load cell (1 kN), controller panel and upper/lower platens (Instron Model 5943). The compression testing setup is illustrated in Figure S3. The compressive modulus was determined from the slope of the stress–strain curve in the linear elastic region, while the compressive strength was taken at 10% strain. For each composite foam, seven rectangular specimens (16 × 16 × 7 mm) were tested, and the average values are reported. Prior to testing, an axial pre-load of 2 N was applied. The specimens were positioned between parallel compression platens and compressed at a constant crosshead speed of 0.7 mm min^{-1} until 50% strain was reached. The procedure was conducted in accordance with ASTM D1621, with the exception that specimen dimensions were smaller than the standard requirement owing to the limited thickness of the extruded foams. Specific compressive modulus and strength values were determined by dividing the measured compressive modulus and strength by the corresponding foam density.

2.3.3 | Dispersion Studies

Transmission electron microscopy (TEM) images were acquired on a JEM 1200 EX microscope (JEOL, USA) operating at a voltage of 80 kV. Prior to acquiring images, pieces of the foam samples were embedded in Spurr's epoxy resin and polymerized

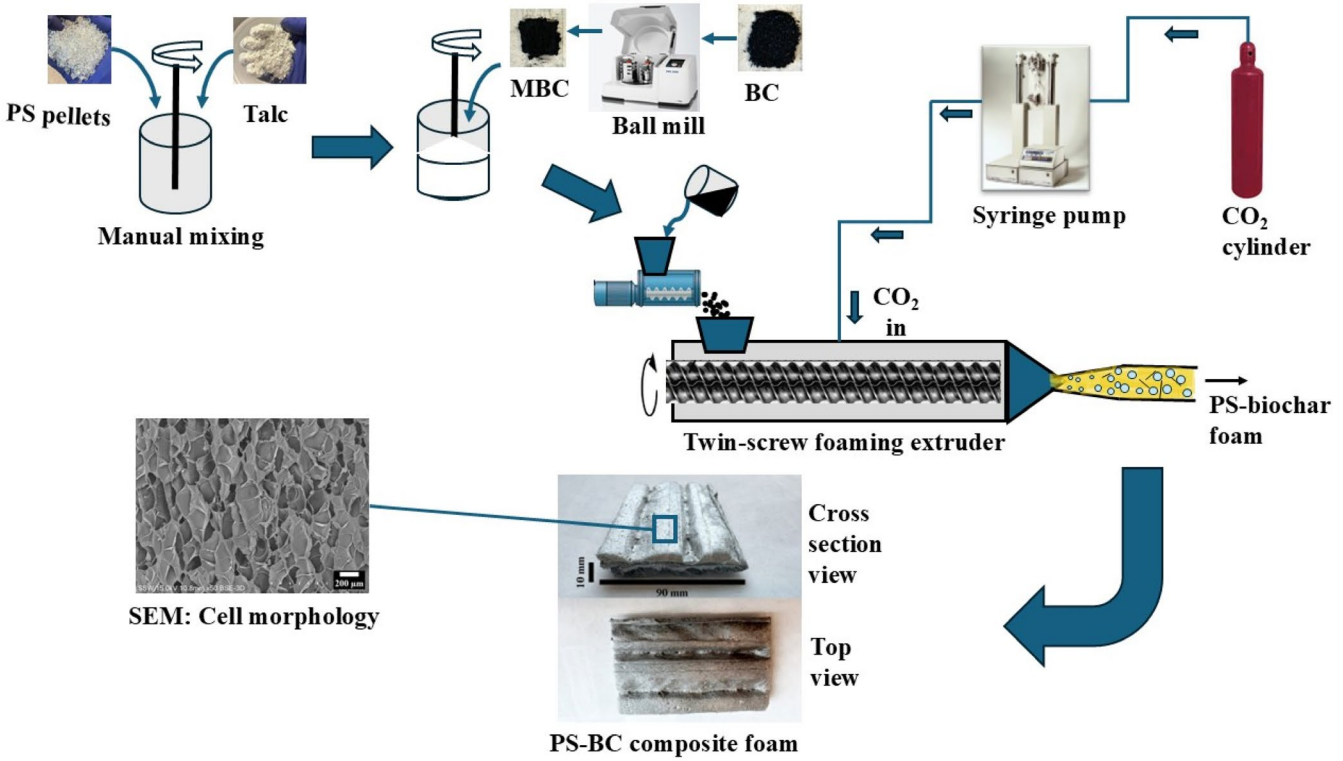

FIGURE 1 | Schematic illustration of the supercritical CO_2-assisted extrusion foaming process used to prepare polystyrene (PS) composite foams containing unmilled biochar (BC) and ball-milled biochar (MBC). [Color figure can be viewed at wileyonlinelibrary.com]

overnight at 60°C. Thin sections were sliced on an ultramicrotome (Leica UCT) and placed on copper grids for viewing under the microscope. The samples were trimmed into rectangular pieces that were suitable for micro-CT analyses. The micro-CT was a Zeiss Xradia 410 Versa. Micro-CT involves passing x-rays through a sample volume and detecting the intensities of the transmitted x-rays. Variations in the sample volume density, such as voids or cracks, cause variations in the x-ray absorption that are expressed as differing greyscale values in the projected image (x-ray radiometric projection image). Multiple projection images are captured at different angles and were subsequently reconstructed into a 3D dataset. Following the acquisition of the datasets, each was processed in Object research system's dragonfly pro software and presented as 3D cubes.

2.3.4 | Biochar Characterization

2.3.4.1 | Structural and Surface Characterization. Biochar was dispersed in ethanol, and a drop of the resulting suspension was deposited onto a glass slide for optical microscopy imaging. For the SEM observation, biochar particles were uniformly mounted on sticky carbon tape and air blown to remove loose powder. High-quality SEM images (50× magnification) and optical microscopy images (4× magnification) of BC and MBC, each with a scale bar, were taken and processed in Fiji (ImageJ) software to measure the particle size distribution [39]. The phase structure of the biochar samples was analyzed using a D2 Phaser powder diffractometer (Bruker, Madison, WI, USA) with Cu Kα radiation ($\lambda = 1.54059$ Å) over a 2θ range of 10°–80°, at a scan rate of 0.1° min^{-1}. The instrument operated at 30 kV and 15 mA. Raman spectroscopy was performed using a RXNI-785 (Kaiser Optical Systems Inc., Ann Arbor, MI, USA) with an excitation wavelength of 785 nm. Fourier-transform infrared (FTIR) spectra were recorded on a Nicolet 6700 FTIR spectrometer (Thermo Scientific) in the wavenumber range of 600–4000 cm^{-1}. The Brunauer–Emmett–Teller (BET) surface area, pore diameter, and pore volume were determined from nitrogen adsorption–desorption isotherms collected at −196°C using a constant-volume adsorption analyzer (Tristar ASAP 2020, Micromeritics Instrument Corp., Norcross, GA, USA) with 99.995% pure N_2 and He (Praxair, Oakville, ON, Canada). Prior to analysis, samples were degassed at 105°C for 12 h. Pore size distributions were derived from the desorption branch using the Barrett–Joyner–Halenda (BJH) method. Energy dispersive x-ray spectroscopy (EDX) coupled with SEM (Hitachi SU3500) operating at 20 kV was used to analyze elemental composition of BC and MBC. Biochar particles were uniformly mounted on sticky carbon tape to ensure complete surface coverage and subsequently positioned on the viewing stage. EDX spectra were acquired from six distinct regions within the imaged area, and the averaged values are reported. Surface hydrophobicity/hydrophilicity of biochar was qualitatively assessed using a water drop penetration test. The test was performed following a procedure adapted from previously reported methods [40]. Biochar powder was placed in a Petri dish to form a loosely packed bed, which was gently tapped to obtain a flat and uniform surface and to minimize the influence of surface roughness. A syringe fitted with a 25-gauge needle was positioned approximately 1 cm above the powder bed. A deionized water droplet with a volume of 0.0048 mL was carefully released onto the surface of the biochar sample, and the drop penetration time was recorded as the moment

when the droplet was no longer visible on the powder surface. Each measurement was conducted in triplicate. Longer drop penetration times were taken to indicate increased hydrophobicity of the biochar, consistent with previously reported observations [41].

2.3.4.2 | Proximate Analysis. The proximate analysis of BC was carried out as per the procedure outlined in a previous study [42]. Moisture content (MC) was determined according to ASTM D1762-84 by drying the samples in an oven at 105°C for 18 h until constant weight was achieved. Volatile matter (VM) was measured using a tube furnace (Lindberg, USA, Model STF54434C) by heating the sample at 950°C for 10 min under nitrogen flow (72 mL min^{-1}) at a heating rate of 13°C/min. Ash content (AC) was evaluated by heating the samples at 750°C for 6 h under a continuous flow of compressed air (72 mL min^{-1}). Fixed carbon (FC) was calculated by subtracting the sum of VM and AC from 100 (dry basis). The pH of biochar samples was measured in a 1:10 (w/v) suspension in deionized water after ultrasonication for 1 h. For all the above measurements, the average of three replicates is reported.

3 | Results and Discussion

3.1 | Characterization of Biochar

3.1.1 | Chemical Composition

Elemental composition by EDX (Table 3) revealed that the biochar consisted mainly of carbon and oxygen, with ball milling increasing oxygen functionalities and exposing mineral-rich phases such as calcium through mechanical activation and surface redistribution, consistent with previous studies [43, 44]. Ash content and fixed carbon remain largely unchanged after short duration ball milling (Table S1).

FTIR spectra (Figure S4a) of the biochar, derived from oak and maple wood residues, exhibited characteristic peaks at 1770, 1480, and 905 cm^{-1}, corresponding to C═O stretching (carbonyl groups), aromatic C═C stretching, and out-of-plane C—H bending, respectively. A weak band observed near 3700 cm^{-1} in the sample is associated with free O—H stretching from surface-bound hydroxyl groups or adsorbed moisture and may also indicate a higher pyrolysis temperature during biochar production [45]. The peak at 1321 cm^{-1} is attributed to phenolic O—H vibrations, while the band near 660 cm^{-1} is attributed to the out-of-plane C—OH or aromatic C—H deformations [46]. A slightly higher peak of phenolic —OH group in MBC could be attributed to surface oxidation due to ball milling and this is also supported by a slight decrease in pH for MBC (Table S1), indicating possible increase in surface acidity [47]. The XRD profiles (Figure S4b) for biochar samples showed a dominant broad hump centered around $2\theta \approx 30°$, characteristic of the (002) diffraction from turbostratic carbon, indicative of an amorphous, partially ordered graphitic structure typical in pyrolyzed woody biochar. Additionally, a minor peak observed at ~$2\theta \approx 37°$ likely originated from residual mineral impurities (e.g., calcite or silicate phases) commonly present in wood-derived biochar and confirmed by elemental analysis, as reported in previous studies [48, 49]. A consistent small feature at $2\theta \approx 50.6°$ appeared and was attributed to an instrumental artifact (ghost peak) rather than a material-related phase, as it does not vary with biochar type or treatment conditions. The XRD results show that milling did not introduce new crystalline phases and does not significantly alter the graphitic structure of biochar but primarily affected particle size and structural disorder.

Raman analysis (Figure S5) showed that the biochar sample had characteristic *D* (~1302 cm^{-1}) and *G* (~1580 cm^{-1}) bands, indicative of disordered sp^2 carbon and graphitic domains, respectively. The calculated intensity ratio (I_D/I_G) decreased slightly from 1.56 for BC to 1.46 for MBC, suggesting a marginal reduction in structural defects or disorder upon ball milling. Kim et al. [50] also observed a decrease in I_D/I_G with longer milling times of biochar, indicating increased graphitization or reduced structural disorder. Water drop penetration test results for BC and MBC are shown in Figure S7. Time-resolved images illustrate the evolution of droplet penetration on the biochar surfaces. For BC, the water droplet remained largely unchanged on the surface for more than 60 s, indicating limited wettability. In contrast, the droplet on MBC gradually penetrated the powder bed and was fully absorbed within approximately 27 s. This faster penetration behavior indicates that MBC is slightly more hydrophilic than BC. Although FTIR analysis confirms that both BC and MBC possess inherently low hydroxyl (—OH) group content, milling increased surface area and exposed additional surface sites, thereby enhancing wettability through physical rather than chemical modifications [51].

3.1.2 | Analysis of Specific Surface Area, Morphology and Particle Size of Biochar

The physicochemical characteristics of biochar influence its performance as a reinforcing filler and nucleating agent in polymer composites. As shown in Table 4, milling of biochar significantly increased its specific surface area (SSA) from 33 to 72 m^2/g, while decreasing both average pore size (from 3.7 to 3.1 nm) and increasing total pore volume (from 0.031

TABLE 3 | Elemental composition of BC and MBC.

	Elemental composition (EDX)				
Biochar type	**C (%)**	**O (%)**	**Mg (%)**	**K (%)**	**Ca (%)**
BC	84.6	10.9	0.1	1.5	2.7
MBC	80.9	13.1	0.1	0.2	5.7

Abbreviations: BC: unmilled biochar, C: carbon, Ca: calcium, K: potassium, MBC: ball-milled biochar, Mg: magnesium, O: oxygen.

TABLE 4 | Physicochemical properties of BC and MBC.

Biochar type	SSA (m^2/g)	PS (nm)	PV (cm^3/g)
BC	33.0	3.7	0.031
MBC	72.1	3.1	0.057

Abbreviations: BC: unmilled biochar, MBC: ball-milled biochar, PS: pore size, PV: pore volume, SSA: specific surface area.

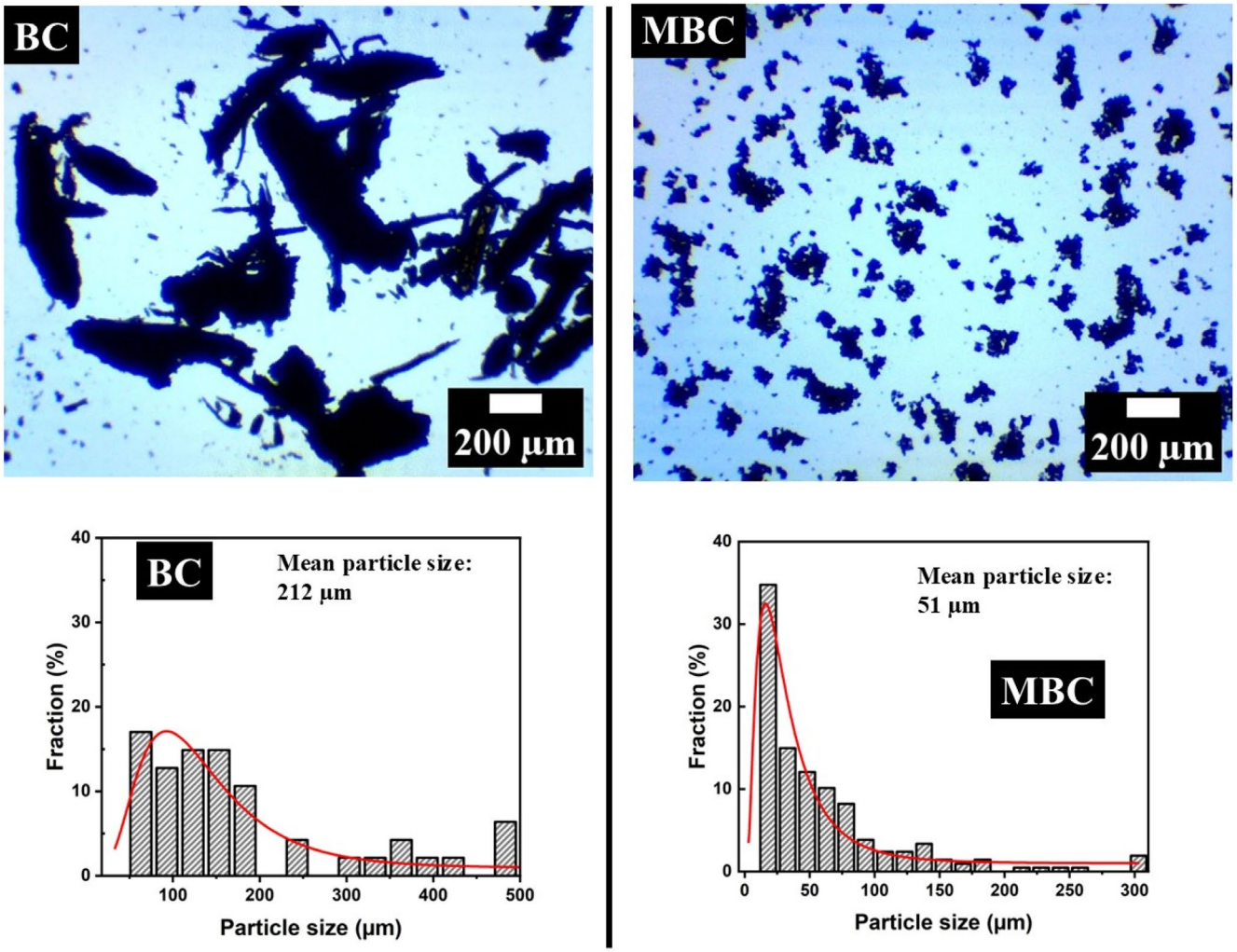

FIGURE 2 | Optical micrographs and particle size distributions of BC and MBC. [Color figure can be viewed at wileyonlinelibrary.com]

to 0.057 cm^3/g). Higher SSA in MBC provides more interfacial contact sites and accessible surface porosity, which can help in nucleation during foaming, act as an insulating barrier to increase thermal resistance, and improve stress transfer within the polymer matrix [52].

The optical micrographs and particle size distributions (Figure 2) showed that ball milling significantly reduced the mean particle size of biochar from 212 µm (BC) to 51 µm (MBC), resulting in a narrower and more uniform particle size distribution. As evident from the images, ball milling effectively reduced the particle size, increasing the surface area and potentially enhancing interfacial interactions within the composites. In addition to optical micrographs, Figure S6 provides the SEM images and particle size distribution of BC and MBC. BC exhibited a coarse, irregular morphology with a mean particle size of 112 µm, whereas the ball-milled biochar (MBC) showed a significantly reduced size (mean: 17 µm) and more homogeneous fine particles, as confirmed by SEM and particle size analysis. The higher mean particle sizes from optical microscopy are attributed to ethanol-dispersed samples containing visible agglomerates, which were measured as larger particles. In contrast, SEM imaging of dry, well-separated particles yielded smaller and more accurate sizes.

3.2 | Cellular Morphology of PS-BC and PS-MBC Composite Foams

3.2.1 | Foaming Expansion Behavior

The details of the extrusion foaming parameter optimization were provided in our previous work [37]. Briefly, key parameters such as sc-CO_2 pressure were optimized through iterative trials to achieve steady-state foaming with uniform cell morphology. The sc-CO_2 pressure significantly influenced CO_2 solubility in the polymer melt and the rate of cell nucleation, with two sc-CO_2 pressures (e.g., 17.3 and 20.6 MPa) producing a foam of consistent quality. This optimization was crucial to balance the gas-polymer solution stability, pressure drop rate, and melt strength, ensuring consistent foam quality. The pilot-scale extrusion foaming setup enabled systematic control over key processing parameters, offering insights relevant to industrial-scale production.

Table S2 shows the apparent densities of pristine and PS composite foams prepared at two sc-CO_2 pressures. BC foam led to a substantial density increase at 20.6 MPa (418.6 kg/m^3), likely due to suppressed cell expansion and thicker cell walls. In contrast, BC foam maintained low densities at both pressures,

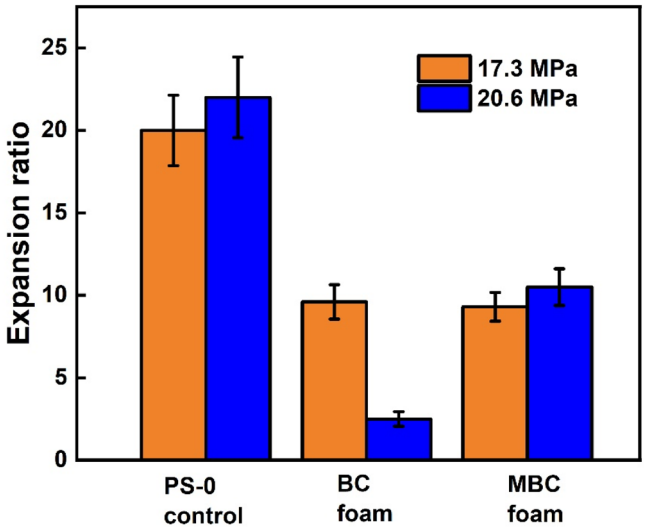

FIGURE 3 | Expansion ratio of PS composite foams with PS-0 control, BC foam and MBC foam at 17.3 and 20.6 MPa sc-CO_2 pressures. [Color figure can be viewed at wileyonlinelibrary.com]

with the lowest (99.1 kg/m^3) achieved at 20.6 MPa, suggesting improved nucleation and cell uniformity that promoted expansion. From Figure 3, the expansion ratio of pristine PS foams (PS-0 control) increased slightly with higher sc-CO_2 pressure (20.6 MPa), reaching values above 22. In contrast, the incorporation of biochar significantly reduced foam expansion across both pressures. Notably, BC foam at 20.6 MPa showed the lowest expansion ratio, indicating limited volume growth and lower foaming. In comparison, MBC foam samples exhibited higher expansion ratios than the BC foam at both sc-CO_2 pressures, suggesting an influence of particle size on foaming behavior. Overall, the addition of biochar reduced the expansion ratio relative to PS-0 control, with the extent depending on both the particle size and sc-CO_2 pressure. Representative images of the BC, MBC, and the prepared composite foams are shown in Figure 4, illustrating the top and cross-sectional morphologies for the foams processed at two different sc-CO_2 pressures.

3.2.2 | Effect of Biochar Particle Size and sc-CO_2 Pressure on the Nucleation in Composite Foam

The mechanism of bubble nucleation in polymer foaming has been extensively explained by previous authors, highlighting the distinction between homogeneous and heterogeneous nucleation pathways [53]. In heterogeneous nucleation, the presence of solid particles lowers the energy barrier for bubble formation, thereby increasing nucleation density.

The combined effect of sc-CO_2 pressure and biochar particle size on foam morphology was evident from the SEM micrographs and corresponding cell size distributions (Figure 5). At 17.3 MPa, the pristine PS foam (PS-0 control) exhibited irregular cell structures with several large, unevenly distributed voids (highlighted in yellow), reflecting a low nucleation density. The cell uniformity improved slightly for BC foam; however, visible large cells remained, indicating limited nucleation efficiency due to the larger BC particle size. In contrast, the MBC foam sample displayed finer and more uniform cells, with significantly more nucleation sites (highlighted in yellow) and reduced average cell size. This enhancement can be attributed to the smaller particle size and higher surface area of MBC, which possibly could have provided more active sites for heterogeneous nucleation and better interaction with dissolved CO_2 molecules [54, 55]. At 20.6 MPa, the improvement in cell structure was more pronounced for the MBC foam sample, which exhibited a narrow and well-defined cell size distribution, supporting the formation of a higher number of nucleated cells. In contrast, the BC foam at this pressure showed a large solid (unfoamed) region (red outline), indicating suppressed foaming and a low expansion ratio, as corroborated by Figure 3. This could be attributed to the large particle size of biochar that disrupted the cell formation and formed thin cell walls which were unable to withstand a high sc-CO_2 pressure [56].

The cell size and cell density analysis (Figure 6) further confirmed the observed trend from the SEM micrographs. Across both the sc-CO_2 pressures, MBC foam samples exhibited significantly smaller average cell sizes and higher cell densities compared to PS-0 control and BC foam foams. Notably, at 20.6 MPa, the MBC foam sample achieved a cell density of approximately 4×10^8 cells cm^{-3}, a 40% increase over the PS-0 control sample (2.5×10^8 cells cm^{-3}). This substantial improvement illustrates the synergistic effect of high sc-CO_2 pressure and fine biochar particles on enhancing nucleation. The increased number of available nucleation sites from the smaller MBC particles, combined with greater gas solubility at higher pressure [57], could have resulted in a high nucleation rate and smaller cell morphology. The narrow distribution of cell sizes in the SEM image for MBC foam at 20.6 MPa visually supports this enhanced nucleation behavior. These results demonstrate that precise control over biochar size and sc-CO_2 pressure can effectively tailor the foam structure for improved performance. Haham et al. [32] also observed that biochar with smaller mean particle size and narrower distribution produced a polylactic acid (PLA) foam with highest cell density and lowest cell size. This was attributed to the mesoporous structure of biochar which created many bubble nucleation sites. Similarly, Jian et al. [58] reported an increase in cell density and a reduction in cell size in PS biocarbon composite foam upon the addition of just 0.05 wt% biocarbon, confirming the role of biochar as an effective nucleating agent.

3.3 | Microstructural Analysis in PS Composite Foams Using TEM and Micro-CT

TEM analysis (Figure 7) confirmed the successful incorporation of biochar into the PS matrix in all foamed samples, regardless of particle size or sc-CO_2 pressure. Carbon-rich regions attributed to biochar were clearly visible in both BC foam and MBC foam, with representative particles highlighted using yellow arrows. A key observation was that biochar particles were frequently located at or near the edges of cells, suggesting their role as effective nucleating agents during bubble formation. Notably, the cell sizes observed in the MBC foam samples were visibly smaller and more uniform compared to those in the BC foam samples. This provides further evidence that reduced biochar particle size enhanced heterogeneous nucleation during the foaming process, contributing to improved cellular structure.

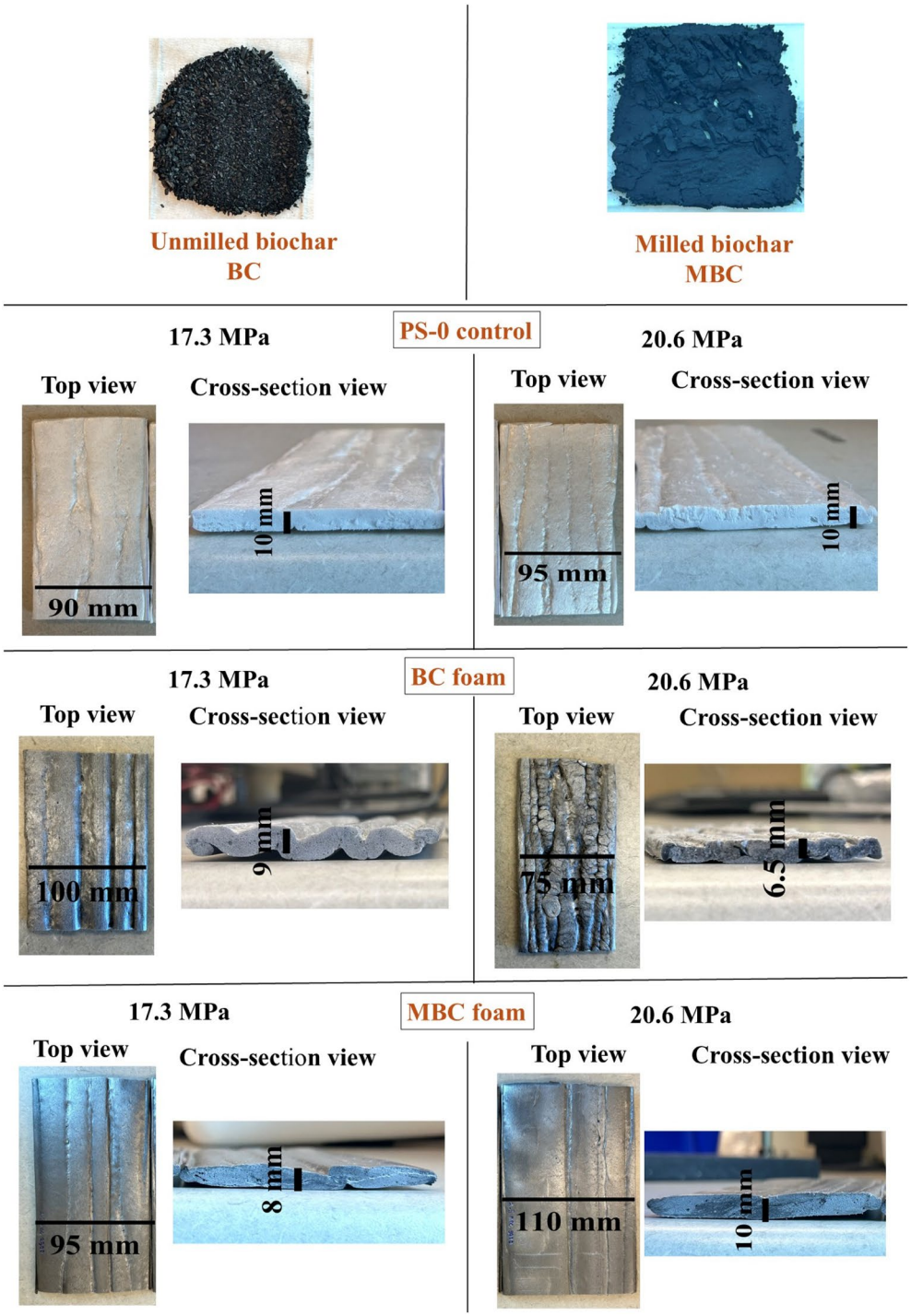

FIGURE 4 | Representative images of unmilled biochar (BC), ball-milled biochar (MBC), and their composite foams processed at the two different sc-CO_2 pressures. [Color figure can be viewed at wileyonlinelibrary.com]

Micro-CT imaging provided a 3D reconstruction of the internal cellular structure and biochar localization within the foamed composites (Figure 8). Carbon-rich regions, highlighted in red, were predominantly located along the cell walls, indicating their role as nucleation sites during foaming. The quantitative volume fraction data is summarized in Table 5. From Figure 8, the MBC foam at 20.6 MPa exhibited a more uniformly distributed presence of biochar particles compared to the BC foam, suggesting improved integration within the matrix. This observation is corroborated by the lower volume fraction of the PS matrix (~5.8%) in MBC foams (Table 5), whereas the BC foam sample at 20.6 MPa displayed a markedly higher matrix volume fraction (~24.5%), indicative of limited expansion and suppressed foaming. Additionally, the higher biochar volume fraction in the MBC foam at high sc-CO_2 pressure indicated more effective particle dispersion. Correspondingly, the BC foam at high pressure revealed a denser and more collapsed cell structure, while the MBC foams maintained larger, well-developed cells, highlighting the influence of reduced particle size on nucleation and foam morphology.

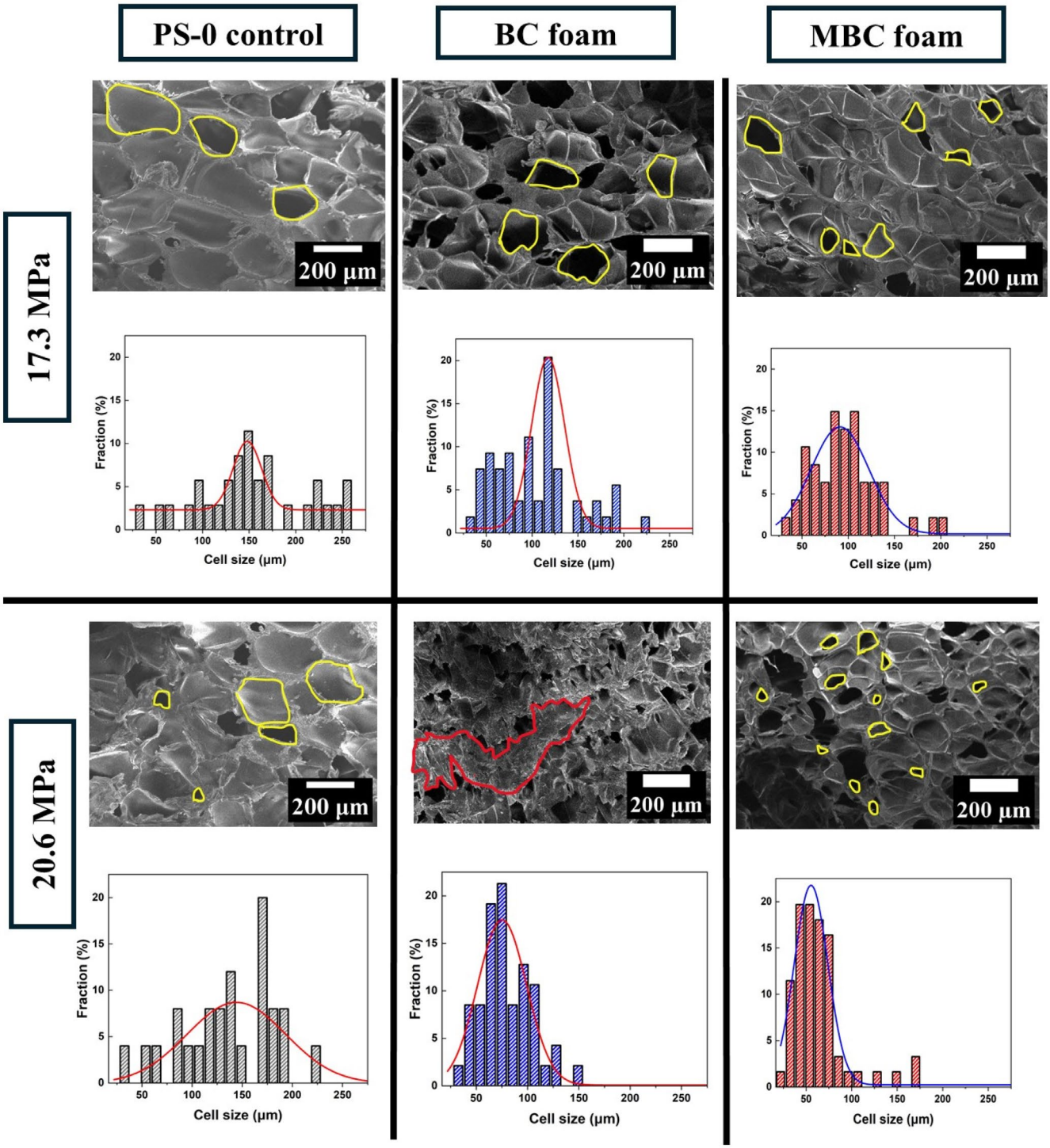

FIGURE 5 | SEM images (top) and corresponding cell size distributions (bottom) of foams extruded at 17.3 and 20.6 MPa sc-CO_2 pressures for PS-0 control, BC, and MBC foam. *Note:* Yellow outlines indicate selected bubble cells, and red outlines highlight unfoamed regions. [Color figure can be viewed at wileyonlinelibrary.com]

3.4 | Thermal and Mechanical Performance

Thermal conductivity is a key property governing the insulation performance of polymer foams. A reduction in thermal conductivity can contribute meaningfully to building energy efficiency, as improved insulation performance can accumulate into measurable energy savings, depending on climate and building type [47]. Figure 9 shows the variation in thermal conductivity for PS-0 control, BC, and MBC foams, prepared at two sc-CO_2 pressures (17.3 MPa and 20.6 MPa). At 17.3 MPa, the similar thermal conductivities of BC and MBC foams can be attributed to comparable cell densities and sizes (Figure 6), suggesting that the higher surface area and reduced particle size of MBC did not translate to increased nucleation under limited CO_2 saturation, thus highlighting the role of sc-CO_2 pressure in realizing the full nucleation potential of MBC [59, 60]. At high sc-CO_2 pressure, MBC foam

showed a ~3.5% reduction in thermal conductivity (32.1 mW/m K) compared to the PS-0 control (33.1 mW/m K), highlighting its effectiveness as an insulating carbon filler. This could be attributed to its high cell density, uniform morphology, and narrow cell size distribution. These microstructural characteristics likely reduced both solid-phase heat conduction paths and gas conductivity, contributing to improved insulation performance [61, 62]. In contrast, BC foam under a high sc-CO_2 pressure exhibited higher thermal conductivity (39.5 mW/m K), likely due to a less uniform cell structure mostly consisting of solid polymer, which increased the thermal transport through the foam matrix.

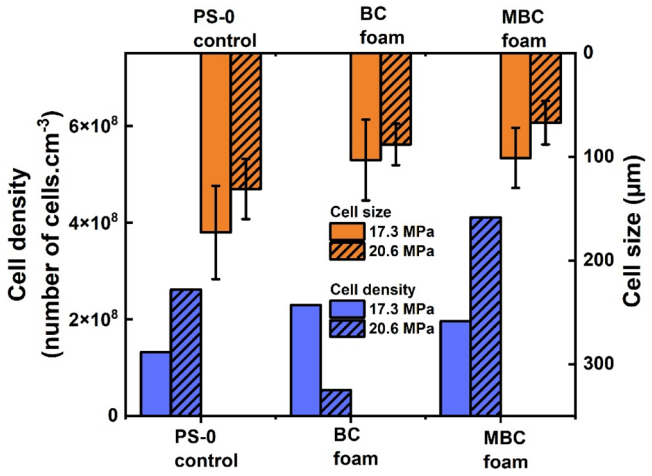

FIGURE 6 | Cell size and cell density of PS-0 control, BC, and MBC foams at 17.3 and 20.6 MPa. [Color figure can be viewed at wileyonlinelibrary.com]

The thermal stability of PS-0 control, BC foam, and MBC foam produced at two different sc-CO_2 pressures (17.3 and 20.6 MPa) was evaluated using TGA, and the corresponding DTG curves are shown in Figure 10, with key parameters summarized in Table S3. All samples exhibited a single major degradation step, characteristic of PS decomposition, indicating similar thermal degradation mechanisms regardless of biochar type or processing pressure [63]. Compared to PS-0 control, BC- and MBC foams showed a slight improvement in thermal stability, evidenced by higher T_{max} values and lower mass loss rates at T_{max}, particularly for BC foam (T_{max} = 411.2°C) and MBC foam (T_{max} = 408.5°C) processed at 17.3 MPa sc-CO_2 pressure. The presence of biochar likely contributed to this stabilization by acting as a thermally stable carbonaceous barrier [64]. At higher sc-CO_2 pressure, a slight

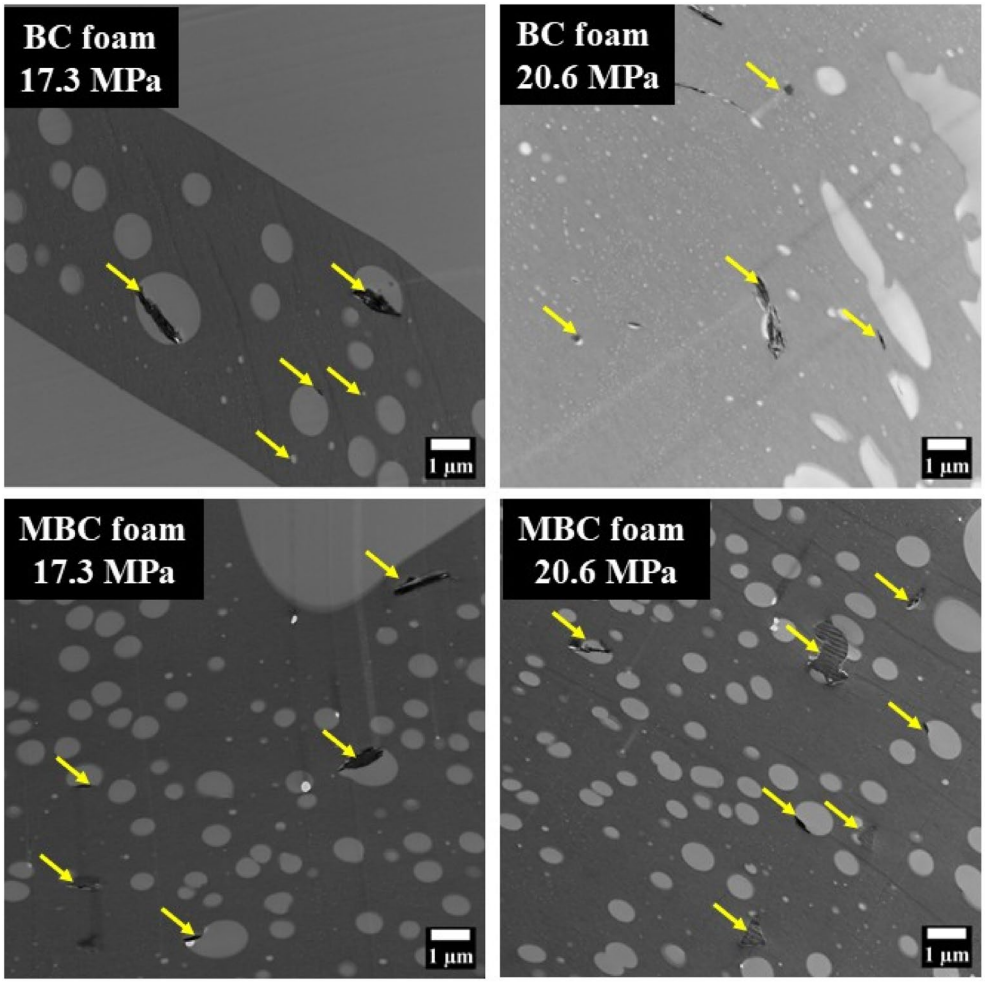

FIGURE 7 | TEM images of PS composite foam at 17.3 and 20.6 MPa sc-CO_2 pressure. *Note:* Yellow arrows represent biochar particles. [Color figure can be viewed at wileyonlinelibrary.com]

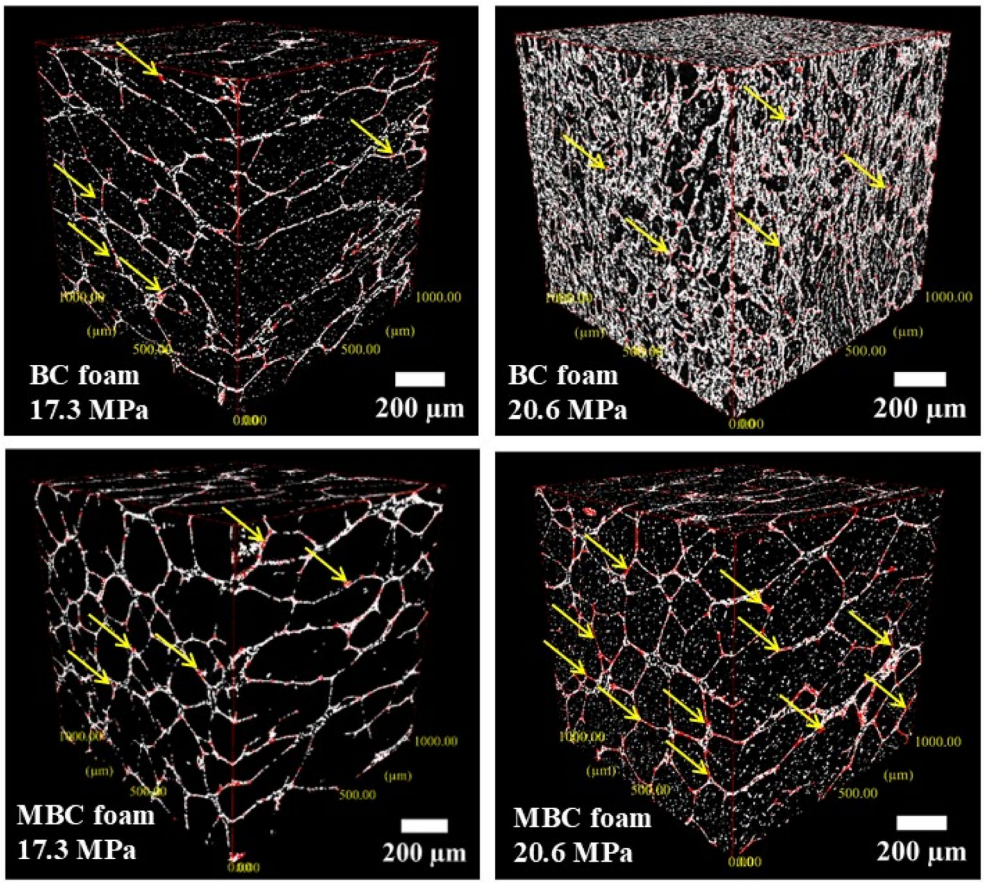

FIGURE 8 | Micro-CT 3D reconstructions of PS composite foams processed at 17.3 and 20.6 MPa. *Note:* Red regions correspond to carbon-rich (biochar) particles concentrated along cell walls; representative locations are highlighted with yellow arrows. [Color figure can be viewed at wileyonlinelibrary.com]

TABLE 5 | Volume fraction (%) of PS matrix and biochar in foamed PS composites from micro-CT analysis.

Sample name	sc-CO_2 pressure (MPa)	Volume fraction of PS matrix (%)	Volume fraction of biochar (%)
BC foam	17.3	3.9	0.8
BC foam	20.6	24.5	1.7
MBC foam	17.3	5.8	0.8
MBC foam	20.6	5.7	1.3

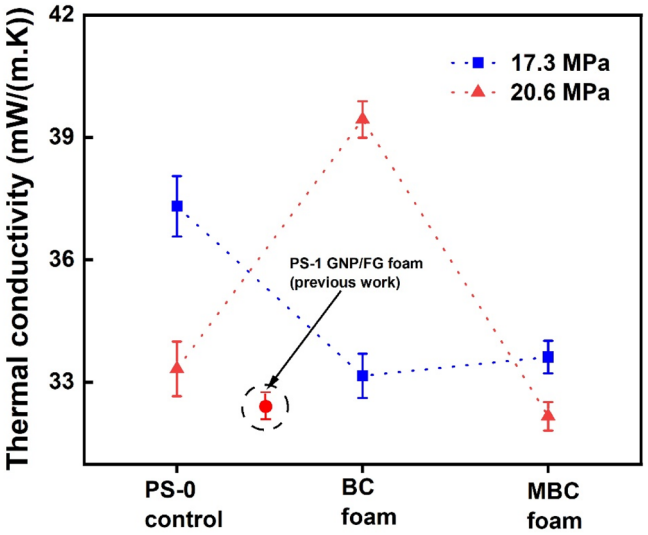

FIGURE 9 | Variation in thermal conductivity of PS-0 control, BC foam, and MBC foam at two different sc-CO_2 pressures. [Color figure can be viewed at wileyonlinelibrary.com]

reduction in T_{max} was observed for both BC and MBC foams, suggesting a pressure-dependent effect on thermal behavior. The overall T_{max} and mass loss rate trends confirmed that biochar addition provided a modest enhancement in the thermal stability of PS composite foams, which remained comparable to PS-0 control foam and support their suitability for thermal insulation applications.

As shown in Figure 11a, the specific compressive modulus increased significantly for MBC foam at 20.6 MPa, reaching ~53 MPa/g cm^{-3}, which is much higher than the PS-0 control (20 MPa/g cm^{-3}). Figure 10b illustrates the effect of BC and MBC on the specific compressive strength of composite foam samples at two sc-CO_2 pressures. At 20.6 MPa, the MBC foam achieved higher strength (~3.8 MPa/g cm^{-3}) compared to PS-0 control (1.6 MPa/g cm^{-3}) and BC foam (1.5 MPa/g cm^{-3}), highlighting

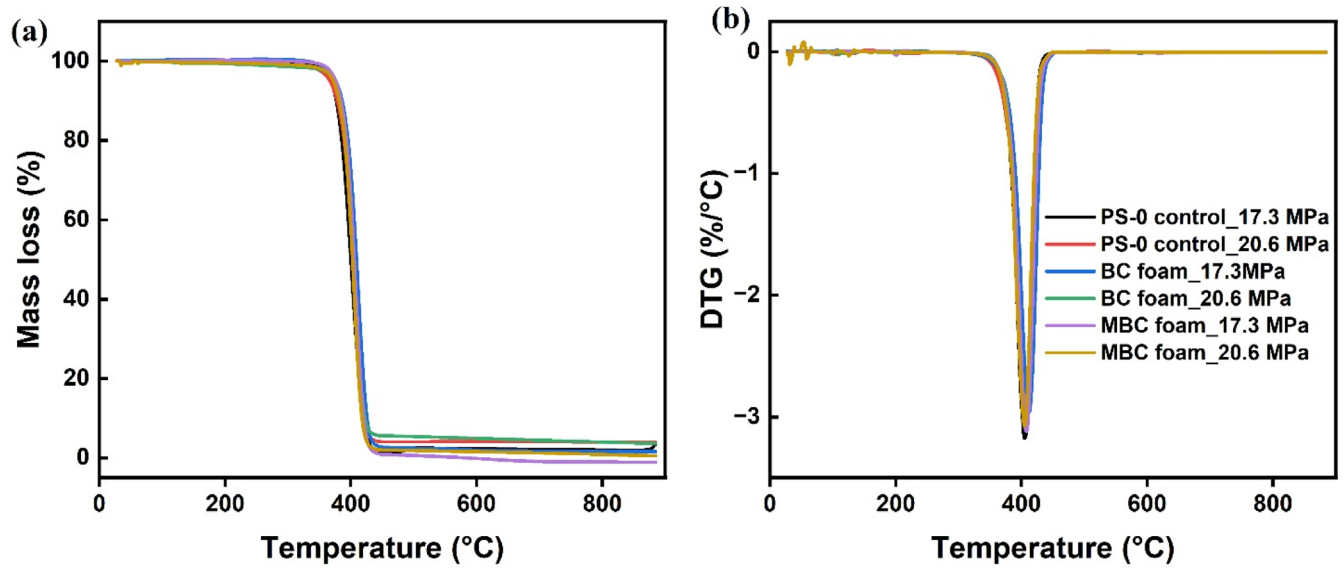

FIGURE 10 | (a) TGA and (b) DTG curves of the PS-BC composite foams at two different sc-CO_2 pressures. [Color figure can be viewed at wileyonlinelibrary.com]

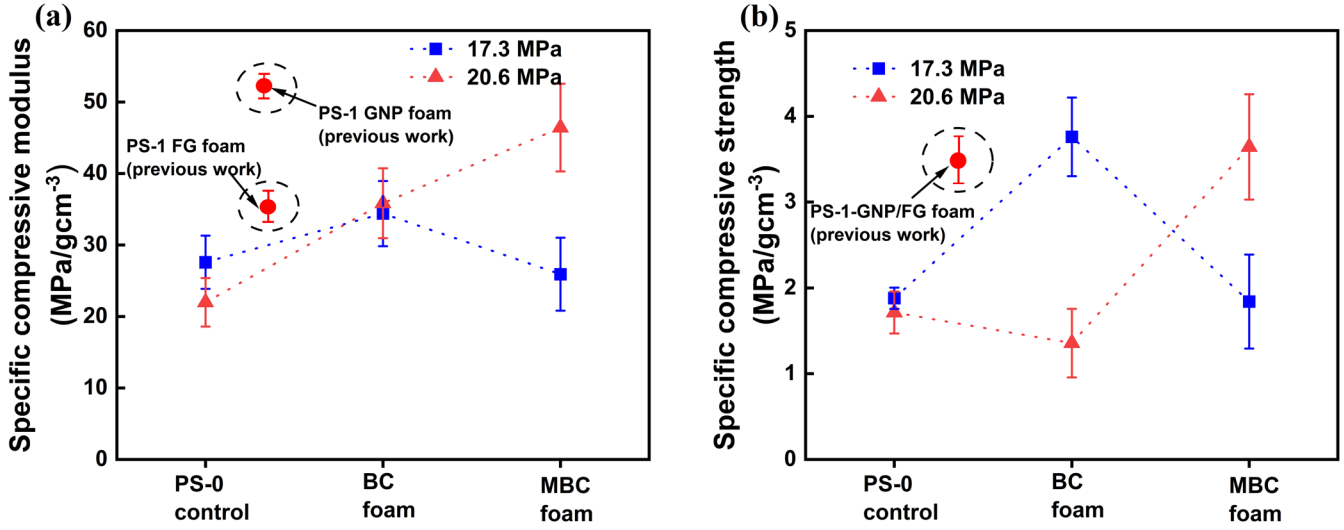

FIGURE 11 | Compression performance of PS-0 control, BC, and MBC foams produced at two different sc-CO_2 pressures. (a) Specific compressive modulus and (b) specific compressive strength. [Color figure can be viewed at wileyonlinelibrary.com]

the reinforcing contribution of MBC. This improvement was attributed to the efficient stress transfer, load distribution, and reinforcing effect of well-dispersed MBC particles in the polymer matrix, combined with a finer and more uniform cell structure achieved at higher sc-CO_2 pressure. Beyond thermal and mechanical performance benefits, MBC offers significant sustainability benefits. Notably, the thermal conductivity of MBC foam at high sc-CO_2 pressure is comparable to GNP- and FG-based foams from our previous work [37] (Figure 11), underscoring its promise as a sustainable, high-performance insulating filler. The compression performance of MBC foam at 20.6 MPa (Figure 11) surpasses that of FG-based foam and approaches GNP-based foam from our previous work [65], demonstrating that MBC is an effective alternative for enhancing stiffness without compromising thermal insulation properties. Compared to expensive fillers like GNP and FG, MBC is low-cost, renewable, and widely available. As a carbon-rich material derived from wood waste, MBC contributes to carbon sequestration in long-lived polymer foams. Its use in building insulation can also support Leadership in Energy and Environmental Design (LEED) certification and the development of low-carbon, green buildings by reducing GHG emissions.

3.5 | Mechanism of Enhanced Nucleation and Cell Structure Refinement in MBC Foams

The proposed mechanism for foaming of PS composite foam with BC, MBC, and role of sc-CO_2 pressure is illustrated in Figure 12. The improved foaming behavior of the PS-MBC composites at high sc-CO_2 pressure was attributed to a synergistic effect between particle surface characteristics and gas saturation. CO_2 molecules are adsorbed on oxygen-containing functional groups and the surface defects on the biochar surface (as identified by

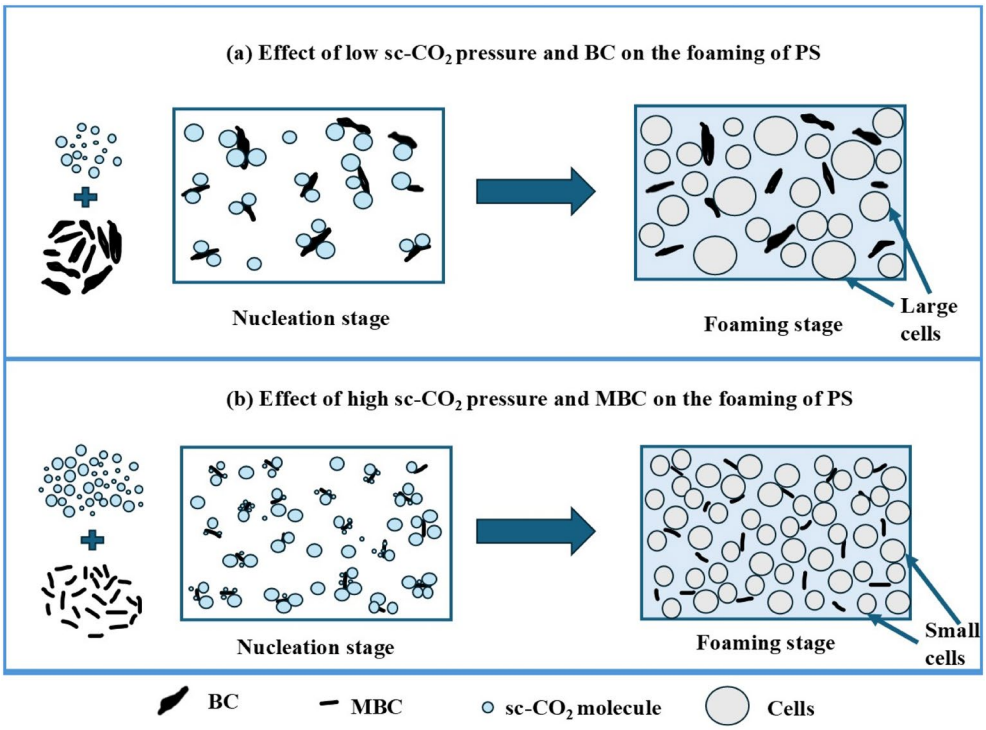

FIGURE 12 | Mechanism illustrating the influence of BC, MBC, and sc-CO_2 pressure on PS nucleation and foaming. [Color figure can be viewed at wileyonlinelibrary.com]

FTIR, EDX, and Raman studies), through weak physisorption and dipole–quadrupole interactions [66, 67]. These interactions promoted the migration and temporary entrapment of CO_2 molecules within the micro- and mesopores of the biochar particles prior to foaming [54]. The MBC, which possessed a higher specific surface area and greater pore volume than BC, can possibly accommodate a larger number of CO_2 molecules on its surface, creating localized regions of elevated gas concentration within the polymer melt. During depressurization, these gas-enriched sites have the potential to act as preferential heterogeneous nucleation centers [68], facilitating rapid bubble formation and uniform cell growth. At high sc-CO_2 pressure, the solubility of CO_2 in the polymer melt increases further, enhancing gas supersaturation and enabling the numerous nucleation sites provided by MBC to be effectively activated. This resulted in a significantly higher cell density and a narrower cell size distribution, as confirmed by SEM analysis of the MBC foams. The fine and homogeneous cellular morphology could have contributed to improved specific compressive strength and reduced thermal conductivity, owing to uniform stress distribution and restricted heat transfer through smaller, well-dispersed cells.

In contrast, the larger particle size and lower surface area of BC could possibly have limited CO_2 adsorption and nucleation efficiency, especially under low sc-CO_2 pressure. Consequently, fewer nucleation sites led to foams with lower cell density, larger and more uneven cells, resulting in higher thermal conductivity and reduced mechanical performance. Interestingly, this mechanism aligns with our previous findings on PS foams reinforced with FG and GNP prepared under similar sc-CO_2 foaming conditions [31]. Although GNP possesses a lower BET surface area (~20 m^2/g) compared with FG (~152 m^2/g), the FG-based foams exhibited higher cell densities at elevated sc-CO_2 pressure. This observation confirms that higher accessible surface area promotes more efficient CO_2 adsorption and heterogeneous nucleation during depressurization. In the present study, the MBC displayed greater surface area (72 m^2/g) than GNP, yet with the added advantage of hierarchical porosity and oxygen-containing surface functionalities. These features likely enhanced CO_2 uptake and localized gas supersaturation, producing finer, denser cell structures. Therefore, the observed synergistic effect between the increased surface area of MBC and elevated sc-CO_2 pressure maximized heterogeneous nucleation, yielding foams with superior structural and functional properties consistent with earlier results and the proposed mechanism.

Table 6 compares the mechanical and thermal insulation (*R*-value and thermal conductivity) performance of the MBC foam developed in this work with previously reported academic PS composite foams and several commercial insulation products. Relative to other academic studies using FG, GNP, or activated carbon fillers, the MBC foam showed the highest specific compressive modulus and maintained comparable or higher specific compressive strength, while also achieving one of the lowest thermal conductivities (32 mW/m K). When benchmarked against commercial insulation foams, the MBC foam exhibited a higher *R*-value than Insulfoam, universal foam EPS, and competitive performance relative to GPS products, although it did not surpass the very low thermal conductivity reported for Foamular NGX. It should be noted that the MBC foam in this study had a higher density than common commercial insulation grades; therefore, further density reduction and optimization of expansion ratio could increase both the *R*-value and the specific compressive strength. Overall, the MBC foam demonstrated superior mechanical performance compared with existing academic PS composites and competitive insulation properties

TABLE 6 | Comparison of mechanical and thermal performance for PS–MBC composite foams with previously reported PS–carbon filler foams and commercial PS insulation products.

Product	Specific compressive modulus ($MPa/g\,cm^{-3}$)	Specific compressive strength ($MPa/g\,cm^{-3}$)	Thermal conductivity (mW/(m K))	*R*-value (inch/BTU·in/h ft² °F)
PS-MBC foam (this work)	48	3.8	32.0	4.5
PS-1 wt% FG [37, 65]	40	3.8	32.1	4.5
PS-1 wt% GNP [37, 65]	33	3.5	32.3	4.5
PS-1 wt% coconut shell AC [25]	20.2	—	34.3	4.2
PS-1 wt% wood AC [69]	—	10	33.9	4.2
Insulfoam [70]	—	3.7	36.2	4.0
Foamular NGX [71]	—	5.3	28.8	5.0
Universal foam EPS [72]	—	3.7	34.4	4.1
Durospan GPS [73]	—	3.5	30.8	4.7

Note: Conversions used for calculating *R*-value are 1 W/m/K = 6.94 BTU·in/h·ft² °F.
Abbreviations: AC: activated carbon, FG: flaked graphite, GNP: graphene nanoplatelets.

relative to commercial materials, highlighting its potential as a sustainable, high-performance alternative.

The lightweight PS-BC/MBC composite foams developed in this study exhibited a favorable combination of low thermal conductivity, enhanced specific compressive strength, and refined cellular microstructure. These characteristics make them promising candidates for load-bearing thermal insulation applications, such as building envelopes, roofing panels, and structural insulation components where both mechanical integrity and thermal efficiency are required. In addition, the incorporation of biochar as a sustainable carbon filler offers potential environmental benefits, including reduced polymer content and the utilization of renewable or waste-derived resources. The compatibility of these composites with continuous sc-CO_2 extrusion further supports their scalability and potential for industrial adoption in energy-efficient construction and insulation systems.

4 | Conclusions

This study demonstrated the successful development of sustainable polystyrene (PS) composite foams reinforced with lignocellulosic-derived biochar using sc-CO_2 extrusion foaming. Ball milling significantly enhanced the specific surface area and pore structure of biochar, improving its dispersion and efficiency as a heterogeneous nucleating agent. The optimized 2.5 wt% ball-milled biochar (MBC) foam processed at 20.6 MPa exhibited a ~40% increase in cell density (4×10^8 cells cm^{-3}) and a narrower cell size distribution (average cell size 75 μm) compared to pristine PS foam (PS-0 control), resulting in highly refined and uniform microcellular architectures. TEM and micro-CT analyses confirmed biochar localization along cell walls and homogeneous distribution throughout the matrix. Mechanistic analysis indicated that the increased surface area of MBC facilitated promoted heterogeneous nucleation due to CO_2 and controlled bubble growth during depressurization. These microstructural improvements translated into a 75% enhancement in specific compressive strength (3.8 $MPa/g\,cm^{-3}$) and a 4% reduction in thermal conductivity (32 mW/m K) as compared to PS-0 control.

Beyond performance gains, this scalable, solvent-free process provides both environmental and industrial benefits. The incorporation of biochar enables long-term carbon sequestration within durable polymer matrices, while the use of sc-CO_2 eliminates harmful chemical blowing agents. Overall, this work demonstrates a practical route to valorize renewable wood residues into high-performance, low-carbon insulation foams, aligning with circular economy principles and advancing sustainable polymer manufacturing.

Author Contributions

Apurv Gaidhani: conceptualization (lead), data curation (lead), formal analysis (lead), investigation (lead), methodology (lead), resources (lead), writing – original draft (lead), writing – review and editing (equal). **Stephan Edwards:** data curation (equal), validation (equal). **William Z. Xu:** conceptualization (equal), data curation (equal), resources (equal). **Lauren Tribe:** formal analysis (lead), funding acquisition (lead), project administration (lead), supervision (lead), validation (equal), writing – review and editing (equal). **Paul Charpentier:** funding acquisition (lead), project administration (lead), supervision (lead), writing – review and editing (equal).

Acknowledgments

The authors would like to acknowledge the financial support from Western Sustainable Impact Fund (WSIF), Mitacs, NSERC CREATE (grant number 401209347), and NSERC Discovery grants. The authors gratefully acknowledge Mr. Ivan Barker from Surface Science Western (SSW) for his valuable support in generating and processing micro-CT images.

Funding

This work was supported by Western Sustainable Impact Fund (WSIF), Mitacs, NSERC CREATE (grant number 401209347), and NSERC Discovery grants.

Conflicts of Interest

The authors declare no conflicts of interest.

Data Availability Statement

The data supporting the findings of this study are included within the manuscript and the Supporting Information.

References

1. M. Aksit, C. Zhao, B. Klose, K. Kreger, H. W. Schmidt, and V. Altstädt, "Extruded Polystyrene Foams With Enhanced Insulation and Mechanical Properties by a Benzene-Trisamide-Based Additive," *Polymers (Basel)* 11 (2019): 268, https://doi.org/10.3390/polym11020268.

2. C. V. Vo and A. N. Paquet, "An Evaluation of the Thermal Conductivity of Extruded Polystyrene Foam Blown With HFC-134a or HCFC-142b," *Journal of Cellular Plastics* 40 (2004): 205–228, https://doi.org/10.1177/0021955X04043719.

3. P. Li, H. Zhang, and L. Chen, "Dynamic Response of EPS Foam in Packaging: Experimental Tests and Constitutive Modeling," *Polymers (Basel)* 17 (2025): 1606, https://doi.org/10.3390/polym17121606.

4. K. Voith, B. Spisák, M. Petrik, et al., "Non-Conventional Reinforced EPS and Its Numerical Examination," *Processes* 11 (2023): 12, https://doi.org/10.3390/pr11010012.

5. H. Yoshihara and M. Maruta, "Measurement of the Shear Properties of Extruded Polystyrene Foam by In-Plane Shear and Asymmetric Four-Point Bending Tests," *Polymers (Basel)* 12 (2020): 47, https://doi.org/10.3390/polym12010047.

6. S. Molleti and D. Van Reenen, "Effect of Temperature on Long-Term Thermal Conductivity of Closed-Cell Insulation Materials," *Buildings* 12 (2022): 425, https://doi.org/10.3390/buildings12040425.

7. A. Rajak, D. A. Hapidin, F. Iskandar, M. M. Munir, and K. Khairurrijal, "Electrospun Nanofiber From Various Source of Expanded Polystyrene (EPS) Waste and Their Characterization as Potential Air Filter Media," *Waste Management* 103 (2020): 76–86, https://doi.org/10.1016/j.wasman.2019.12.017.

8. S. Elmozy, Y. Elkhayat, and E. Eldarwish, "The Thermal and Energy Performance Comparison of Extruded Polystyrene Foam Insulation for an Apartment Building in Different Climate Zones,Egypt," *Journal of Engineering Research* 7 (2023): 284–293, https://doi.org/10.21608/erjeng.2023.235588.1241.

9. Resources Canada N, "Keeping the Heat in," 2025, https://naturalresources.canada.ca/energy-efficiency/home-energy-efficiency/keeping-heat.

10. S. Danov, J. Carbonell, J. Cipriano, and J. Martí-Herrero, "Approaches to Evaluate Building Energy Performance From Daily Consumption Data Considering Dynamic and Solar Gain Effects," *Energy and Buildings* 57 (2013): 110–118, https://doi.org/10.1016/j.enbuild.2012.10.050.

11. H. X. Zhao and F. Magoulès, "A Review on the Prediction of Building Energy Consumption," *Renewable and Sustainable Energy Reviews* 16 (2012): 3586–3592.

12. J. R. Zhao, R. Zheng, J. Tang, H. J. Sun, and J. Wang, "A Mini-Review on Building Insulation Materials From Perspective of Plastic Pollution: Current Issues and Natural Fibres as a Possible Solution," *Journal of Hazardous Materials* 438 (2022): 129449.

13. "Tracking Buildings," 2023, https://www.iea.org/energy-system/buildings.

14. L. Pérez-Lombard, J. Ortiz, and C. Pout, "A Review on Buildings Energy Consumption Information," *Energy and Buildings* 40 (2008): 394–398, https://doi.org/10.1016/j.enbuild.2007.03.007.

15. S. B. Sadineni, S. Madala, and R. F. Boehm, "Passive Building Energy Savings: A Review of Building Envelope Components," *Renewable & Sustainable Energy Reviews* 15 (2011): 3617–3631, https://doi.org/10.1016/j.rser.2011.07.014.

16. D. Cuthbertson, U. Berardi, C. Briens, and F. Berruti, "Biochar From Residual Biomass as a Concrete Filler for Improved Thermal and Acoustic Properties," *Biomass & Bioenergy* 120 (2019): 77–83, https://doi.org/10.1016/j.biombioe.2018.11.007.

17. O. Das, A. K. Sarmah, and D. Bhattacharyya, "Biocomposites From Waste Derived Biochars: Mechanical, Thermal, Chemical, and Morphological Properties," *Waste Management* 49 (2016): 560–570, https://doi.org/10.1016/j.wasman.2015.12.007.

18. S. Gupta and H. W. Kua, "Factors Determining the Potential of Biochar as a Carbon Capturing and Sequestering Construction Material: Critical Review," *Journal of Materials in Civil Engineering* 29 (2017): 4017086, https://doi.org/10.1061/(asce)mt.1943-5533.0001924.

19. U. Berardi, "The Impact of Temperature Dependency of the Building Insulation Thermal Conductivity in the Canadian Climate," in *Energy Procedia* (Elsevier Ltd, 2017), 237–242.

20. C. C. Dymond, B. D. Titus, G. Stinson, and W. A. Kurz, "Future Quantities and Spatial Distribution of Harvesting Residue and Dead Wood From Natural Disturbances in Canada," *Forest Ecology and Management* 260 (2010): 181–192, https://doi.org/10.1016/j.foreco.2010.04.015.

21. C. Mvolo, "Matching Woody Residues With Application," 2025, https://natural-resources.canada.ca/forest-forestry/forest-industry-trade/woody-residues.

22. T. A. Tengku Yasim-Anuar, L. N. Yee-Foong, A. A. Lawal, et al., "Emerging Application of Biochar as a Renewable and Superior Filler in Polymer Composites," *RSC Advances* 12 (2022): 13938–13949.

23. A. Gaidhani, L. Tribe, and P. Charpentier, "Polystyrene Carbon Composite Foam With Enhanced Insulation and Fire Retardancy for a Sustainable Future: Critical Review," *Journal of Cellular Plastics* 59 (2023): 419–453, https://doi.org/10.1177/0021955X231215753.

24. A. G. Adeniyi, J. O. Ighalo, and D. V. Onifade, "Production of Biochar From Elephant Grass (Pernisetum Purpureum) Using an Updraft Biomass Gasifier With Retort Heating," *Biofuels* 12 (2021): 1283–1290, https://doi.org/10.1080/17597269.2019.1613751.

25. L. Jian, T. Fan, M. Weng, et al., "A Comparative Study of the Effect of Multidimensional Carbon Fillers on Polystyrene Using Supercritical Carbon Dioxide Foaming," *Diamond and Related Materials* 130 (2022): 109495, https://doi.org/10.1016/j.diamond.2022.109495.

26. A. G. Adeniyi, S. A. Abdulkareem, E. C. Emenike, et al., "Mechanical and Chemical Characterization of Biochar-Reinforced Polystyrene Composites," *BMC Chemistry* 18 (2024): 246, https://doi.org/10.1186/s13065-024-01365-2.

27. C. Das, S. Tamrakar, A. Kiziltas, and X. Xie, "Incorporation of Biochar to Improve Mechanical, Thermal and Electrical Properties of Polymer Composites," *Polymers (Basel)* 13 (2021): 2663, https://doi.org/10.3390/polym13162663.

28. E. O. Ogunsona, M. Misra, and A. K. Mohanty, "Sustainable Biocomposites From Biobased Polyamide 6,10 and Biocarbon From Pyrolyzed Miscanthus Fibers," *Journal of Applied Polymer Science* 134 (2017): 44221, https://doi.org/10.1002/app.44221.

29. E. O. Ogunsona, M. Misra, and A. K. Mohanty, "Impact of Interfacial Adhesion on the Microstructure and Property Variations of Biocarbons Reinforced Nylon 6 Biocomposites," *Composites Part A, Applied Science and Manufacturing* 98 (2017): 32–44, https://doi.org/10.1016/j.compositesa.2017.03.011.

30. M. Bartoli, R. Arrigo, G. Malucelli, A. Tagliaferro, and D. Duraccio, "Recent Advances in Biochar Polymer Composites," *Polymers (Basel)* 14 (2022): 2506.

31. A. G. Adeniyi, S. A. Abdulkareem, J. O. Ighalo, D. V. Onifade, S. A. Adeoye, and A. E. Sampson, "Morphological and Thermal Properties of Polystyrene Composite Reinforced With Biochar From Elephant Grass (*Pennisetum purpureum*)," *Journal of Thermoplastic Composite Materials* 35 (2020): 1532–1547, https://doi.org/10.1177/0892705720939169.

32. H. Haham, A. Riscoe, C. W. Frank, and S. L. Billington, "Effect of Bubble Nucleating Agents Derived From Biochar on the Foaming Mechanism of Poly Lactic Acid Foams," *Applied Surface Science Advances* 3 (2021): 100059, https://doi.org/10.1016/j.apsadv.2021.100059.

33. K. Uram, M. Kurańska, J. Andrzejewski, and A. Prociak, "Rigid Polyurethane Foams Modified With Biochar," *Materials* 14 (2021): 5616, https://doi.org/10.3390/ma14195616.

34. M. Aboughaly and B. Acharya, "Enhancing the Potential of Polymer Composites Using Biochar as a Filler: A Review," *Polymers* 15 (2023): 3981.

35. F. A. Almeida, H. Beyrichen, N. Dodamani, R. Caps, A. Müller, and R. Oberhoffer, "Thermal Conductivity Analysis of a New Sub-Micron Sized Polystyrene Foam," *Journal of Cellular Plastics* 57 (2021): 493–515, https://doi.org/10.1177/0021955X20943101.

36. W. Zheng and Y. Pang, "Utilization of Supercritical CO_2 in Continuous Extrusion Foaming and Polymer Processing," accessed 12 August 2025, https://english.nimte.cas.cn/rh/rp/201603/t20160330_161315.html.

37. A. Gaidhani, G. Min, W. Z. Xu, L. Tribe, and P. Charpentier, "Synergistic Effects of Carbon Additives and Supercritical CO_2 on Cell Morphology and Thermal Insulation of Extruded Polystyrene Composite Foam," *Polymer Engineering and Science* 65 (2025): 4170–4185, https://doi.org/10.1002/pen.27283.

38. A. Gaidhani, G. Min, L. Tribe, and P. Charpentier, "Supercritical CO_2-Foamed Polystyrene Composites Containing Wood-Derived Biochar for Sustainable Thermal Insulation," *RSC Sustainability* (2025), https://doi.org/10.1039/d5su00884k.

39. R. A. Mensah, D. Wang, V. Shanmugam, et al., "Fire Behaviour of Biochar-Based Cementitious Composites," *Composites Part C: Open Access* 14 (2024): 100471, https://doi.org/10.1016/j.jcomc.2024.10047.

40. L. Briens and B. Bowden-Green, "A Comparison of Liquid Binders for Drum Granulation of Biochar Powder," *Powder Technology* 367 (2020): 487–496, https://doi.org/10.1016/j.powtec.2020.03.065.

41. A. Fazzalari, C. Briens, and L. Tribe, "An Investigation of Drum Granulation of Post-Pyrolysis Washed Biochar," *Canadian Journal of Chemical Engineering* 102 (2024): 574–584, https://doi.org/10.1002/cjce.25087.

42. D. Aller, S. Bakshi, and D. A. Laird, "Modified Method for Proximate Analysis of Biochars," *Journal of Analytical and Applied Pyrolysis* 124 (2017): 335–342, https://doi.org/10.1016/j.jaap.2017.01.012.

43. H. Nan, R. Huang, X. Zhang, and C. Wang, "How Does Ball-Milling Elevate Biochar as a Value-Added Peroxydisulfate Activator for Antibiotics Removal?," *Industrial Crops and Products* 214 (2024): 118569, https://doi.org/10.1016/j.indcrop.2024.118569.

44. L. Li, Y. Xie, K. Chen, et al., "Adsorption Characteristics of Ball Milling-Modified Chinese Medicine Residue Biochar Toward Quercetin," *ACS Omega* 9 (2024): 11658–11670, https://doi.org/10.1021/acsomega.3c09016.

45. J. Bedia, M. Peñas-Garzón, A. Gómez-Avilés, J. J. Rodriguez, and C. Belver, "A Review on the Synthesis and Characterization of Biomass-Derived Carbons for Adsorption of Emerging Contaminants From Water," *C* 4 (2018): 63, https://doi.org/10.3390/c4040063.

46. M. A. McCall, J. S. Watson, J. S. W. Tan, and M. A. Sephton, "Biochar Stability Revealed by FTIR and Machine Learning," *ACS Sustainable Resource Management* 2 (2025): 842–852, https://doi.org/10.1021/acssusresmgt.5c00104.

47. H. Lyu, B. Gao, F. He, et al., "Effects of Ball Milling on the Physicochemical and Sorptive Properties of Biochar: Experimental Observations and Governing Mechanisms," *Environmental Pollution* 233 (2018): 54–63, https://doi.org/10.1016/j.envpol.2017.10.037.

48. M. L. Bornø, J. O. Eduah, D. S. Müller-Stöver, and F. Liu, "Effect of Different Biochars on Phosphorus (P) Dynamics in the Rhizosphere of *Zea mays* L. (Maize)," *Plant and Soil* 431 (2018): 257–272, https://doi.org/10.1007/s11104-018-3762-y.

49. K. W. Jung, M. J. Hwang, K. H. Ahn, and Y. S. Ok, "Kinetic Study on Phosphate Removal From Aqueous Solution by Biochar Derived From Peanut Shell as Renewable Adsorptive Media," *International Journal of Environmental Science and Technology* 12 (2015): 3363–3372, https://doi.org/10.1007/s13762-015-0766-5.

50. D. Y. Kim and G. B. Jung, "Effects of Pyrolysis and Ball-Milling on the Physicochemical and Rhodamine B Removal Characteristics of Rice-Bran-Derived Biochar," *Applied Sciences* 13 (2023): 4288, https://doi.org/10.3390/app13074288.

51. Q. Zhang, J. Wang, H. Lyu, Q. Zhao, L. Jiang, and L. Liu, "Ball-Milled Biochar for Galaxolide Removal: Sorption Performance and Governing Mechanisms," *Science of the Total Environment* 659 (2019): 1537–1545, https://doi.org/10.1016/j.scitotenv.2019.01.005.

52. H. Baniasadi, L. Äkräs, Z. Paganelli, et al., "Can Biochar Fillers Advance the Properties of Composites? Early-Stage Characterization and Life Cycle Assessment of Novel Polyamide/Biochar Biocomposites," *Environmental Research* 275 (2025): 121446, https://doi.org/10.1016/j.envres.2025.121446.

53. J. Colton and N. Suh, "The Nucleation of Microcellular Thermoplastic Foam With Additives: Part I: Theoretical Considerations," *Polymer Engineering and Science* 27 (1987): 482–492.

54. C. Yang, M. Wang, Z. Xing, Q. Zhao, and G. Wu, "A New Promising Nucleating Agent for Polymer Foaming: Effects of Hollow Molecular-Sieve Particles on Polypropylene Supercritical CO2 Microcellular Foaming," *RSC Advances* 8 (2018): 20061–20067, https://doi.org/10.1039/c8ra03071e.

55. M. P. Motloung, V. Ojijo, J. Bandyopadhyay, and S. S. Ray, "Cellulose Nanostructure-Based Biodegradable Nanocomposite Foams: A Brief Overview on the Recent Advancements and Perspectives," *Polymers (Basel)* 11 (2019): 1270.

56. A. A. Maamoun, R. M. Abouomar, T. M. El-Basheer, et al., "Improving the Acoustic Performance of Flexible Polyurethane Foam Using Biochar Modified by (3-Aminopropyl)Trimethoxysilane Coupling Agent," *Scientific Reports* 14 (2024): 18382, https://doi.org/10.1038/s41598-024-68039-w.

57. H. Perera, V. Rahmanian, M. Sohail, S. Mohammadkhah, A. Ahuja, and S. A. Khan, "Using Supercritical CO_2 for Viscosity Reduction of Polymers: A Data-Driven Modeling Approach for Predicting the Diffusive Properties of Polystyrene Melt," *Industrial & Engineering Chemistry Research* 64 (2025): 16700–16710, https://doi.org/10.1021/acs.iecr.5c01740.

58. R. Jian, P. Shahi, M. Semeniuk, et al., "Acoustic Absorption Properties of Polystyrene-Pyrolytic *Pinus resinosa* Composite Foams Prepared by Torsion-Induced Extrusion," *Macromolecular Materials and Engineering* 607 (2021): 1–9, https://doi.org/10.1002/mame.202100622.

59. M. Dippold and H. Ruckdäschel, "Influence of Pressure-Induced Temperature Drop on the Foaming Behavior of Amorphous Polylactide (PLA) During Autoclave Foaming With Supercritical CO_2," *Journal of Supercritical Fluids* 190 (2022): 105734, https://doi.org/10.1016/j.supflu.2022.105734.

60. E. Reverchon and S. Cardea, "Production of Controlled Polymeric Foams by Supercritical CO_2," *Journal of Supercritical Fluids* 40 (2007): 144–152, https://doi.org/10.1016/j.supflu.2006.04.013.

61. P. Gong, P. Buahom, M. P. Tran, M. Saniei, C. B. Park, and P. Pötschke, "Heat Transfer in Microcellular Polystyrene/Multi-Walled

Carbon Nanotube Nanocomposite Foams," *Carbon* 93 (2015): 819–829, https://doi.org/10.1016/j.carbon.2015.06.003.

62. O. V. Soloveva, S. A. Solovev, Y. V. Vankov, and R. Z. Shakurova, "Experimental Studies of the Effective Thermal Conductivity of Polyurethane Foams With Different Morphologies," *PRO* 10 (2022): 2257, https://doi.org/10.3390/pr10112257.

63. A. H. Farha, A. F. Al Naim, and S. A. Mansour, "Thermal Degradation of Polystyrene (PS) Nanocomposites Loaded With Sol Gel-Synthesized ZnO Nanorods," *Polymers* 12 (2020): 1935, https://doi.org/10.3390/POLYM12091935.

64. A. Y. Elnour, A. A. Alghyamah, H. M. Shaikh, et al., "Effect of Pyrolysis Temperature on Biochar Microstructural Evolution, Physicochemical Characteristics, and Its Influence on Biochar/Polypropylene Composites," *Applied Sciences* 9 (2019): 1149, https://doi.org/10.3390/app9061149.

65. A. Gaidhani, S. Edwards, L. Tribe, and P. Charpentier, "Enhancing Mechanical Performance of Polystyrene Carbon Composite Foams Through Supercritical CO_2 Foaming: An Experimental Study," *Journal of Thermoplastic Composite Materials* (2025): 08927057251401189, https://doi.org/10.1177/08927057251401189.

66. X. Cheng, Z. Qie, H. Xiang, et al., "Engineering Nitrogen and Oxygen Functionalities in Naturally Sourced Activated Carbon for Multicomponent Gas Adsorption," *Scientific Reports* 15 (2025): 28102, https://doi.org/10.1038/s41598-025-13430-4.

67. S. Guo, Y. Li, Y. Wang, L. Wang, Y. Sun, and L. Liu, "Recent Advances in Biochar-Based Adsorbents for CO_2 Capture," *Carbon Capture Science & Technology* 4 (2022): 100059, https://doi.org/10.1016/j.ccst.2022.100059.

68. J. Tatibouët and R. Gendron, "Heterogeneous Nucleation in Foams as Assessed by In-Line Ultrasonic Measurements," *Journal of Cellular Plastics* 41 (2005): 57–72, https://doi.org/10.1177/0021955X05050214.

69. C. Zhang, B. Zhu, and L. J. Lee, "Extrusion Foaming of Polystyrene/Carbon Particles Using Carbon Dioxide and Water as Co-Blowing Agents," *Polymer* 52 (2011): 1847–1855, https://doi.org/10.1016/j.polymer.2011.02.016.

70. Insulfoam, "Technical Data Sheet: Insulfoam Expanded Polystyrene (EPS) Insulation Insulfoam," 2024 Carlisle Construction Materials, https://www.insulfoam.com/insulation-brochures-literature/.

71. Owens Corning, *Technical Data Sheet: FOAMULAR NGX Extruded Polystyrene (XPS) Insulation* (Owens Corning Insulating Systems, LLC, 2020), https://www.owenscorning.com/en-ca/technical-resource-library/products/foamular-ngx.

72. Universal Foam Products, *EPS Data Sheet: Universal Foam Expanded Polystyrene Insulation* (Universal Construction Foam Products, 2024), https://univfoam.com/learning-center/eps-r-values/.

73. DuroSpan, *Technical Data Sheet: DuroSpan GPS R5 Graphite Polystyrene Insulation* (Atlas Roofing Corporation, 2024), https://www.plastifab.com/products/durospan-gps-insulation/durospan-gps-r5.html.

Supporting Information

Additional supporting information can be found online in the Supporting Information section. **FIGURE S1:** app70441-sup-0001-Supinfo.docx. **FIGURE S2:** app70441-sup-0001-Supinfo.docx. **FIGURE S3:** app70441-sup-0001-Supinfo.docx. **FIGURE S4:** app70441-sup-0001-Supinfo.docx. **FIGURE S5:** app70441-sup-0001-Supinfo.docx. **FIGURE S6:** app70441-sup-0001-Supinfo.docx. **FIGURE S7:** app70441-sup-0001-Supinfo.docx. **TABLE S1:** app70441-sup-0001-Supinfo.docx. **Table S2:** app70441-sup-0001-Supinfo.docx. **TABLE S3:** app70441-sup-0001-Supinfo.docx.